Received 18 February 2024; revised 21 March 2024; accepted 1 April 2024. Date of publication 4 April 2024; date of current version 24 April 2024.

Digital Object Identifier 10.1109/OJCOMS.2024.3385021

Multibeam Beamforming for Direct Radiating Arrays in Satellite Communications Using Genetic Algorithm

JUAN ANDRÉS VÁSQUEZ-PERALVO (Member, IEEE), JORGE QUEROL (Member, IEEE), FLOR ORTÍZ (Member, IEEE), JORGE LUIS GONZÁLEZ RIOS (Member, IEEE), EVA LAGUNAS (Senior Member, IEEE), LUIS MANUEL GARCÉS-SOCORRÁS (Member, IEEE), JUAN CARLOS MERLANO DUNCAN (Senior Member, IEEE), MARCELE O. K. MENDONÇA (Member, IEEE), AND SYMEON CHATZINOTAS (Fellow, IEEE)

Interdisciplinary Centre for Security, Reliability, and Trust (SnT), University of Luxembourg, 1855 Luxembourg City, Luxembourg

CORRESPONDING AUTHOR: J. A. VÁSQUEZ-PERALVO (e-mail: juan.vasquez@uni.lu)

This work was supported by the European Space Agency (ESA) funded under Contract 4000134522/21/NL/FGL named "Satellite Signal Processing Techniques Using a Commercial Off-The-Shelf AI Chipset (SPAICE)."

ABSTRACT Recent advancements in onboard satellite communication have enhanced the capability of dynamically modifying the radiation pattern of a Direct Radiating Array (DRA). This is crucial not only for conventional communication satellites like Geostationary Orbit (GEO) but also for those in lower orbits such as Low Earth Orbit (LEO). Key design factors include the number of beams, beamwidth, Effective Isotropic Radiated Power (EIRP), and Side Lobe Level (SLL) for each beam. However, a challenge arises in multibeam scenarios when trying to simultaneously meet requirements for the aforementioned design factors which are reflected as uneven power distribution. This leads to over-saturation, especially in centrally located antenna elements due to the activation times per beam, commonly referred to as activation instances. In response to this challenge, this paper presents a method to balance the activation instances across antenna elements for each required beam. Our focus is on beams operating at 19 GHz on a CubeSat positioned 500 km above the Earth's surface. We introduce a Genetic Algorithm (GA)-based algorithm to optimize the beamforming coefficients by modulating the amplitude component of the weight matrix for each antenna element. A key constraint of this algorithm is a limit on activation instances per element, which avoids over-saturation in the Radio Frequency (RF) chain. Additionally, the algorithm accommodates beam requirements such as beamwidth, SLL, pointing direction, and total available power. With the previous key design factors, the algorithm will optimize the required genes to address the desired beam characteristics and constraints. We tested the algorithm's effectiveness in three scenarios using an 8×8 DRA patch antenna with circular polarization, arranged in a triangular lattice. The results demonstrate that our algorithm not only meets the required beam pattern specifications but also ensures a uniform activation distribution across the antenna array.

INDEX TERMS Antennas, beamforming, direct radiating array, satellite communications.

I. INTRODUCTION

SATELLITE Communications play a key role, serving as a foundation of connectivity and two-way information exchange from Earth to space. This technology enables communication across long distances and in remote locations where terrestrial networks are either unavailable or economically unfeasible to implement. Moreover, satellite communications facilitate a wide range of applications, including global broadcasting, multicasting, weather forecasting, navigation, emergency communications, space

mission communications, and interplanetary mission communications, just to mention a few. Their importance keeps growing due to an increasingly interconnected world, where the demand for real-time data and communication is ever-present.

CubeSats, a subset of satellites deployed in various orbits, are miniaturized satellites offering several distinct advantages over traditional satellite designs [1]. Beyond the evident benefits such as reduced costs, expedited development times, ease of launch, and standardization, CubeSats are particularly attractive due to their compact size. This compactness makes them ideal for frequent and versatile applications and facilitates their use in high-frequency operations where the size of the components, like antennas, is reduced.

A crucial component of CubeSats is the payload antenna, which is essential in shaping radiation patterns to meet specific requirements. These patterns are designed according to targeted coverage areas, and the necessary Effective Isotropic Radiated Power (EIRP), enabling efficient satellite service across diverse regions. Different antenna architectures have been considered in the literature oriented on the use in CubeSats. For instance, planar antennas, particularly patch antennas [2], [3], [4], along with arrays of patch antennas [5], [6], [7], and deployable patch antennas [8]. Besides planar types, reflector-based antennas are also utilized [9]. Now if we focus on antennas that allow for beam pattern synthesis, the list narrows to arrays allowing phase shift and amplitude adjustments in each antenna element, such as phased arrays [10], [11], reflect arrays [12], [13], and transmit arrays [14].

Beam pattern synthesis is a key element in antenna design, which can be broadly categorized into three groups: amplitude-only synthesis, phase-only synthesis, and combined amplitude-and-phase synthesis. In amplitude-only synthesis, the power received by each antenna element is adjusted according to the desired radiation pattern. This approach often employs analytical methods using established taper distributions like Chebyshev, Taylor, Hamming, or Hann for amplitude values [15]. Non-deterministic techniques, such as Genetic Algorithms (GA) [16], [17] and Particle Swarm Optimization (PSO) [18], are also utilized when analytical methods are not available. The second category, phase-only synthesis, focuses on shaping the beam or reducing interference by exclusively modifying the phase of the array elements. Various works have targeted beam shaping [19] and interference reduction [20] within this framework. Finally, the combined amplitude-and-phase synthesis incorporates both amplitude and phase adjustments. Deterministic methods such as Linearly Constrained Minimum Variance (LCMV) and Minimum Variance Distortionless Response (MVDR) [21] fall into this category, along with hybrid approaches that blend deterministic and non-deterministic methods [22].

To achieve the desired tapering in each antenna element without incurring high manufacturing costs or increasing the risk of failure due to step amplitude variation, array thinning emerges as a superior method. This approach not only maintains cost-effectiveness but also preserves the capability for beam steering in the antenna array [17]. Array thinning is a concept used in the field of antennas, more specifically in phase arrays, where the main aim is to deactivate certain elements to obtain a desired radiation pattern. Besides the previous radiation pattern, there are other goals for thinning arrays like reducing complexity, costs, weight, heat, computational requirements, and size [15].

The integration of GA for array thinning has been extensively studied over the past 50 years, yielding significant insights for the design of antennas, especially for on-board applications [23]. This body of work can be broadly categorized into two main types: fixed thinned arrays and 1-bit reconfigurable amplitude arrays. The first category includes arrays where the thinned elements have been replaced by a 50-ohm load or completely removed. Within this domain, research has focused on achieving desired Side Lobe Level (SLL) and gain in single and dual-band phase arrays, employing various geometries such as rectangular [24], and circular [25], [26]. Moreover, efforts not only consider the lattice of the array but also the asymmetry of the desired beams [27]. Additionally, studies have explored multibeam systems [28] and interleaved arrays for mono-pulse systems [29]. Conversely, 1-bit reconfigurable amplitude array category applies array thinning to synthesize beams, considering constraints like SLL, beamwidth, nulls, and EIRP for single beam scenarios. Under this category, authors have researched the application in linear arrays [30], and planar arrays [17], [31].

However, these studies predominantly focus on synthesizing either a single beam or multiple beams using different physical sections of the array or one beam at a time as is the case of analog beamforming, without optimizing the entire array for each beam at the same time as is the case of digital beamforming scenarios. Furthermore, a critical gap in the literature is the lack of emphasis on even power distribution across array elements due to the activation instances, or constraints on overall on-board power limits for multibeam pattern generation, particularly in CubeSats.

To address these issues, this paper focuses on a multibeam scenario, generating beams with specified beamwidth and SLL. It specifically addresses the challenge of avoiding saturation in the central elements (activation of an element in all the beams) of a thinned array, which typically experience the highest levels of saturation. The approach involves activating underutilized or inactive elements to address a certain activation instance per element. Additionally, this work also takes into account the constraint of limited available power, while still meeting the requirements for beamwidth, SLL, and activation instances. To summarize the contributions of the presented paper are:

- A step-by-step guide for antenna dimensioning based on the minimum coverage area,

- An algorithm based on GA that synthesizes beams in a multiple beam scenario considering required beamwidth, SLL, and power.
- The algorithm will also evenly distribute activation instances across the whole array to reduce the over-saturation of the RF chain.

This paper is organized as follows. Section II describes the array antenna dimensioning for a CubeSat scenario, focusing on the Field of View (FoV), satellite altitude, and the minimum coverage area. This section also includes the design of the unit cell for this specific scenario. In Section III, we detail the extracted parameters of the radiation pattern, facilitating comparison with the desired radiation pattern in the algorithm stage. Section IV presents the description of the array thinning algorithm, specifically the GA, for both single-beam and multi-beam scenarios. The results and analysis of the multi-beam scenario, considering three different cases, are detailed in Section V. Finally, Section VI offers conclusions and discusses future work derived from this research.

II. ANTENNA DIMENSIONING AND DESIGN

We consider the downlink of an Non-Geostationary Orbit (NGSO) satellite, which is equipped with a Direct Radiating Array (DRA). The design of the DRA starts with the array dimensioning, polarization, dimensions constraints, mutual coupling, frequency range, and bandwidth.

A. ARRAY DIMENSIONING

Array dimensioning involves the determination of three key parameters: the half-power beamwidth, denoted as $\theta_{\text{-3dB}}$, the inter-element spacing, represented by d, and the number of elements in each dimension, N_x and N_y. Detailed calculations of these parameters, adapted to the specific conditions of the current scenario, are presented in the subsequent paragraphs.

The scenario under study involves a DRA mounted on the face of a 1U CubeSat, orbiting in a Low Earth Orbit (LEO) at an altitude of $h = 500$ km above the Earth's surface. The coverage area required on Earth must be adaptable, with a minimum symmetric diameter of 100 km. This requirement results in a coverage area $A_C = 7521.22$ km^2. Figure 1 depicts a representation of this scenario and a set of variables that will allow determining the required beamwidth based on the coverage area.

Utilizing A_C we can estimate the half of the satellite coverage angle α_c, viewed from the earth center, by applying the spherical cap Equation (1),

$$\alpha_c = \cos^{-1}\left(-\frac{A_c}{2\pi R_e^2} + 1\right), \tag{1}$$

where R_e is the radius of the Earth and equal to 6317 km. Then, applying the law of sines, we can express Equation (2) to solve for θ, being θ the half of the angle corresponding to the $\theta_{-3\text{dB}}$ needed in the antenna,

$$\sin\theta = \frac{R_e}{R_e + h}\sin(\theta + \alpha_c). \tag{2}$$

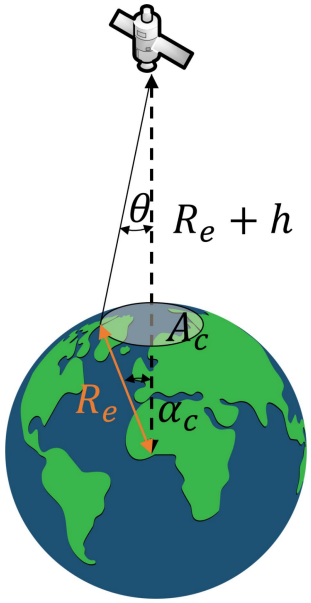

FIGURE 1. Satellite scenario to determine the beamwidth viewed from the satellite antenna.

The numerical results obtained show that the antenna needs to provide $\theta_{-3\text{dB}} = 9.32°$.

Determining the antenna's inter-element spacing hinges on the requirement that no grating lobe should intersect the antenna's FoV across the Earth's surface. To accomplish this, the FoV itself can be computed through the equation outlined in (3), which is derived from the depiction in Figure 1.

$$FoV = \tan^{-1}\frac{R_e}{R_e + h}. \tag{3}$$

The result of applying the previous formula gives a FoV $= 42.43°$, which is the input for the inter-element space calculation in Equation (4) [15],

$$d = \frac{\lambda_0}{2\sin(FoV)}. \tag{4}$$

As a result, the antennas must be separated $d = 0.74\ \lambda_0$ from each other to warranty scanning capabilities without having any grating lobes inside the FoV.

The conclusive step involves dimensioning the antenna number of elements per dimension N_x, N_y using Equation (5) [22],

$$N_x = N_y = \frac{0.886\lambda_0}{\eta\theta_{-3\text{dB}}d}, \tag{5}$$

where λ_0 is the free space wavelength, and η is the antenna efficiency. Since the antenna will work at an operational frequency f_0 =19 GHz, maximum efficiency, and to give a reasonable margin to avoid operating in the limit of the beamwidth, the total number of elements per dimension is $N_x = N_y = 8$.

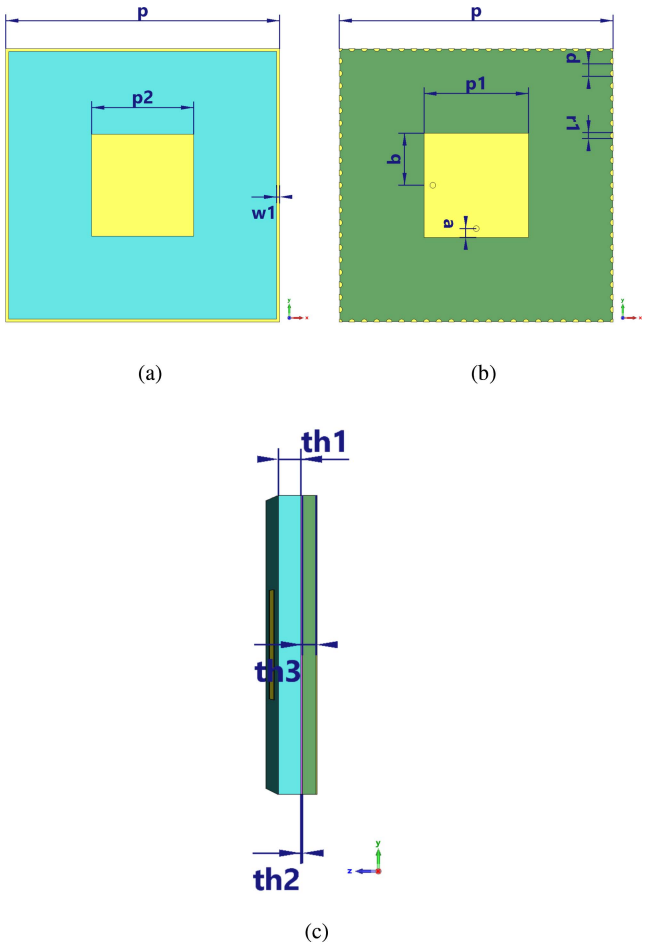

FIGURE 2. Proposed antenna dimensions: a) upper layer view, b) middle layer view, c) lateral view.

TABLE 1. Proposed unit cell dimensions.

Parameter	Value mm	Description
p	11.68	Period of the unit cell
p1	3.6	Width of the bottom patch
p2	3.51	Width of the upper patch
w1	0.1	Width of the cage frame
a	0.3	Center of the pin to the edge of the patch
b	1.8	Position of the pin in the bottom patch
d	0.425	Period of the cage pins
r1	0.1	Raiodus of the cage pins
th1	0.75	Thickness of the upper substrate
th2	0.05	Thickness of the prepreg
th3	0.45	Thickness of the bottom substrate

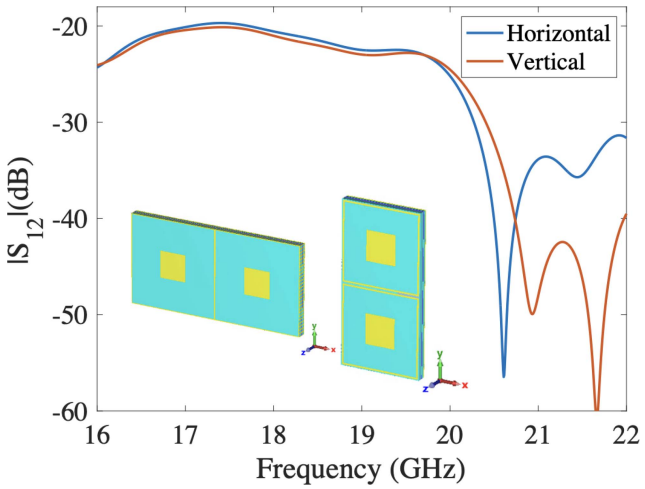

FIGURE 3. Mutual Coupling simulation of the unit cell when the a neighbour unit cell is located vertically and horizontally.

B. UNIT CELL DESIGN AND SIMULATION

The unit cell selected for this application is a patch antenna due to its compactness, which makes it perfect for CubeSat, its circular polarization capabilities, and low cost. Considering the inherent limitation in the bandwidth of a single-layer patch antenna due to its resonant nature, our design incorporates a double-layered patch to significantly enhance the bandwidth. Furthermore, to mitigate the mutual coupling typically introduced by the double-layer configuration, we have incorporated an upper frame in each unit cell. This frame is connected through vias to the ground plane, effectively reducing mutual coupling. A detailed illustration of the antenna and its various components is provided in Figure 2.

To address the frequency requirements of the antenna an optimization has been carried out constraining the optimizer to use standard and realizable values for substrates, trace width, space width, via size, and tolerances. Detailed dimensions of the designed unit cell are presented in Table 1.

The substrates employed in the unit cell design uses RO4003 material, known for its reliability in high-frequency applications. The feeding mechanism employed in our design is a double pin feed approach. In this feed structure we can delay one port by 90 degrees to produce either the Right-Hand Circular Polarization (RHCP) or the Left-Hand Circular Polarization (LHCP). This choice was made to optimize signal distribution and minimize losses, ensuring the robustness and efficiency of our antenna design.

Furthermore, in this analysis, as we opt to use the array factor formula instead of full-wave simulations for estimating the array's total radiation pattern, it becomes crucial to account for the mutual coupling between antenna elements. To this end, we have conducted a mutual coupling analysis across two distinct scenarios: vertically and horizontally adjacent unit cells. The findings, illustrated in Figure 3, demonstrate that in both configurations, the mutual coupling remains below -20 dB. This level of coupling ensures minimal power transfer between neighboring unit cells, thereby preserving the integrity of the array's performance and safely using the array factor formula to estimate the array radiation pattern.

The unit cell has been simulated using the time domain solver in CST microwave studio considering a proper meshing to ensure that the results are as reliable as possible.

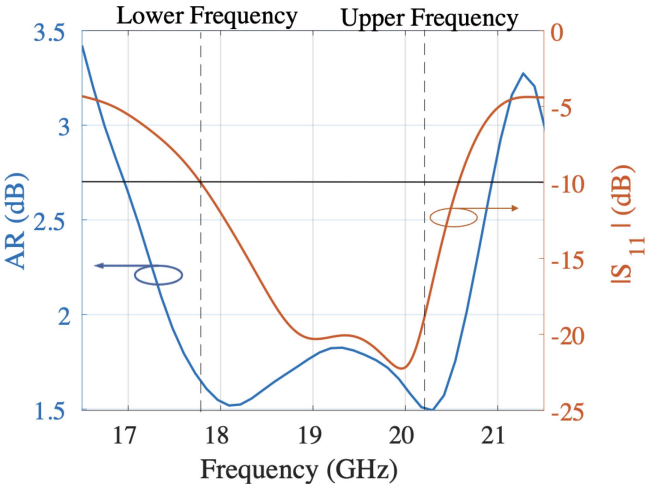

FIGURE 4. $|S_{11}|$ and axial ratio simulation results of the proposed unit cell antenna.

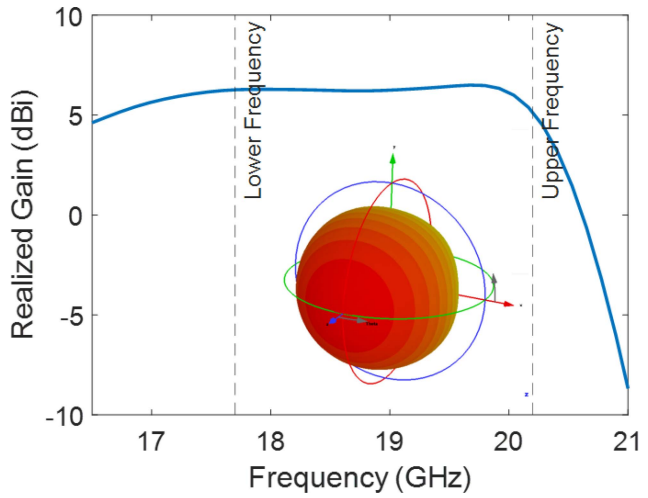

FIGURE 5. Simulated gain in the frequency band of interest and radiation pattern at 19 GHz of the design antenna.

Figure 4 shows the obtained $|S_{11}|$ and axial ratio, which are under -10dB and 3 dB, respectively, in the frequency band of interest (from 17.7 to 20.2 GHz).

In addition, the simulated gain in the targeted band is also presented along with the 3D radiation pattern in Figure 5. The results show a stable gain trend as the frequency increases until it reaches the upper-frequency band, where it starts decreasing.

C. ARRAY CONFIGURATION, DESIGN, AND SIMULATION

In this design, the array is configured in a hexagonal lattice layout, a choice motivated by the packing density of elements within a given area, improving that of square or rectangular configurations. This arrangement effectively minimizes the emergence of grating lobes, as detailed by [32]. According to the Array Dimensioning section, the configuration will incorporate an 8×8 matrix of elements, with an inter-element spacing of $0.74\lambda_0$, predicated on the assumption of minimal mutual coupling. This presumption, as stated before, is supported by the encapsulated design of each unit cell and the fact that the spacing between elements is greater than $0.5\lambda_0$. Additionally, the overall dimensions of the array are approximately 94 mm, rendering it compatible with a single CubeSat face. The total radiation pattern, denoted AP, is accurately determined by the product of the array factor and the element pattern, as mathematically depicted in Equation (6).

$$AP(\theta,\phi) = E_{UC}(\theta,\phi) \times AF(\theta,\phi), \tag{6}$$

where $E_{UC}(\theta,\phi)$ is the element pattern and $AF(\theta,\phi)$ is the array factor, calculated using Equation (7) [15].

$$\mathrm{AF}(\theta,\phi) = \sum_{m=0}^{M_x}\sum_{n=0}^{N_y}\sum_{p=0}^{P_z} W_{mnp} e^{\mathrm{j}(m)(\kappa d_x \sin(\theta)\cos(\phi))} \times e^{\mathrm{j}(n)(\kappa d_y \sin(\theta)\sin(\phi))} \times e^{\mathrm{j}(p)(\kappa d_z \cos(\theta))}, \tag{7}$$

where M_x is the number of elements in the x-direction, N_y is the number of elements in the y-direction, P_z is the number of elements in the z-direction, κ is the wave number, d_x is the period in the x-direction, d_y is the period in the y-direction, d_z is the period in the z-direction, θ and ϕ are the evaluating angles, and W_{mnp} is the weight matrix entry of index (m, n, p). Furthermore, considering the implementation of beam scanning angles and amplitude control over the antenna elements, the term W_{mnp} is expanded as detailed in Equation (8).

$$W_{mnp} = |W_{mnp}| e^{-\mathrm{j}\kappa(\sin\theta_0(md_x\cos\phi_0 + nd_y\sin\phi_0) + pd_z cos\theta_0)}, \tag{8}$$

where (θ_0, ϕ_0) represent the scanning angles. The aforementioned formula applies to any array configuration, irrespective of the location of the antenna elements. However, in our study, the equation is simplified to suit the context of working exclusively with planar arrays. The total process to obtain the total radiation pattern is visually depicted in Figure 6.

The radiation pattern resulting from the array factor in azimuth and elevation coordinates, achieved using a triangular lattice and an all-one matrix for W, is depicted in Figure 7. The results show that the radiation pattern has a maximum of 26.25 dBi of directivity when the array is pointing at the broadside, which produces a SLL of around 13.3 dB. Furthermore, analyzing the beamwidth we can see that it reaches around 8.35°, which is slightly lower than the desired due to the upper rounding of the antenna elements.

III. RADIATION PATTERN PARAMETERS

This section describes the antenna parameters that will be considered in the optimization algorithm, which is detailed in the subsequent section. The parameters included in the optimization process are: beamwidth, SLL, EIRP, and overall power consumption.

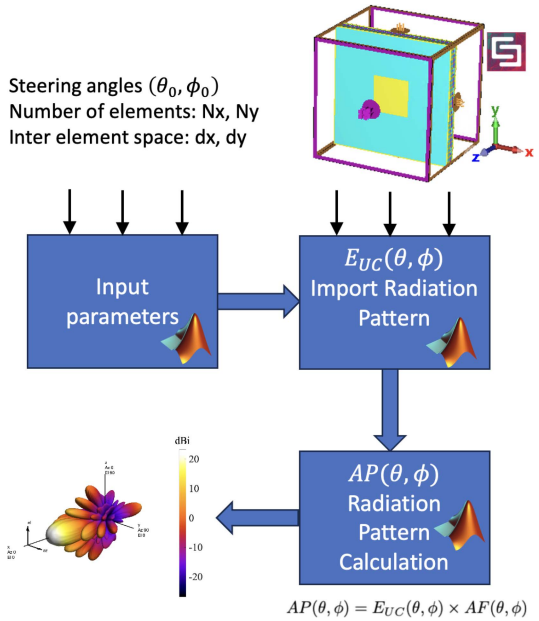

FIGURE 6. Block diagram of the process to obtain the final radiation pattern based on the array factor and the antenna radiation pattern.

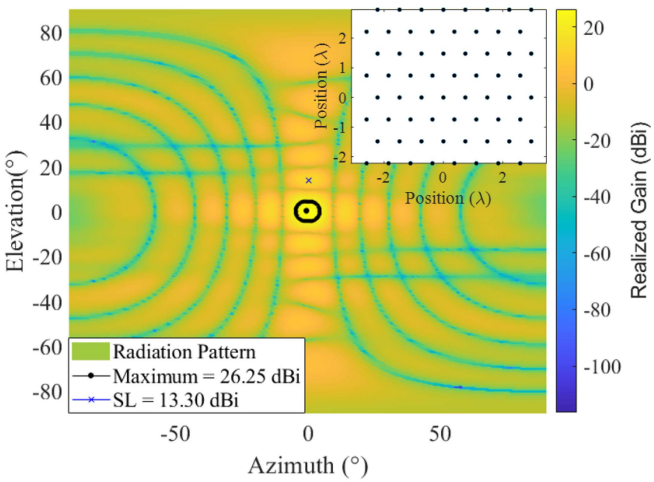

FIGURE 7. Simulated radiation pattern, calculated using the array factor formula, for arrays composed of the designed unit cells arranged in a triangular lattice.

A. BEAMWIDTH

The beamwidth of each beam in the radiation pattern is calculated as the average value derived from various radiation pattern cuts. For each cut, the beamwidth is determined by calculating the angular difference between the maximum and minimum angles at which the -3dB beamwidth point occurs. This calculation method is specified in Equation (9).

$$\theta^b_{-3dB} = |\Theta^b_{-3_{dB,2}} - \Theta^b_{-3_{dB,1}}|, \tag{9}$$

where $\Theta_{-3_{dB,1}}$, $\Theta_{-3_{dB,2}}$ are the angles at which the radiated power drops to half.

B. SIDE LOBE LEVELS

The SLL is defined as the ratio of the maximum amplitude of the side lobes to the maximum amplitude of the main lobe, and it is expressed in decibels (dB), as shown in Equation (10):

$$\mathrm{SLL}^b(\mathrm{dB}) = 20\log_{10}\left(\frac{\mathrm{AP}^b_{\mathrm{SL,max}}}{\mathrm{AP}^b_{\mathrm{max}}}\right), \tag{10}$$

In this optimization process, which involves activating or deactivating antenna elements, the SLL may not always be located in a principal cut but can appear at a random angular position. Therefore, the optimizer will examine the entire radiation pattern to identify the second-highest maximum, thereby determining the overall SLL, excluding those located outside the FoV.

C. EFFECTIVE ISOTROPIC RADIATED POWER

The calculation of the EIRP per beam can be computed by considering the Equation (11)

$$EIRP^b = G^b(\theta, \phi)(\mathrm{dB}) + T_x(\mathrm{dBW}), \tag{11}$$

where $G(\theta, \phi)$ is the gain of the optimized antenna and T_x is the transmitted power of the array, that can be calculated as indicated in Equation (12):

$$T_x(\mathrm{dBW}) = \sum_{m=0}^{M}\sum_{n=0}^{N}\sum_{p=0}^{P} 10\log_{10}\left(|W_{mnp}|^2\right), \tag{12}$$

and the gain can be computed using Equation (13)

$$G^b(\theta, \phi)(\mathrm{dB}) = 10\log_{10}\left[\eta \cdot D^b(\theta, \phi)\right], \tag{13}$$

where the directivity $D(\theta, \phi)$ is defined as

$$D^b(\theta, \phi) = \frac{4\pi}{\int_0^{2\pi}\int_0^{\pi} \mathrm{AP}^b(\theta, \phi)^2 \sin(\theta)\mathrm{d}\theta\mathrm{d}\phi}. \tag{14}$$

IV. ARRAY THINNING ALGORITHM

A. SINGLE BEAM SCENARIO

As a first approach to reach the multibeam scenario, we can define an algorithm that computes the activated beams to reach a desired θ_{-3dB}, and SLL. To accomplish this we need to define a cost function that can relate the calculated beamwidth ($\theta_{-3\mathrm{dB_c}}(W_{m\times n})$), and minimum Side Lobe Level ($\mathrm{SLL_c}(W_{m\times n})$) with the desired counterparts ($\theta_{-3\mathrm{dB_{Az_o}}}$), ($\mathrm{SLL_o}(W_{m\times n})$), respectively. The cost function used for this scenario is presented in Equation (15).

$$\min_{W_{m\times n}} Z_1(W_{m\times n}) + Z_2(W_{m\times n}) \tag{15}$$

where:

$$\begin{cases} Z_1 = \sum_{r=1}^{R}\left(\frac{|\theta_{-3\mathrm{dB_r}}(W_{m\times n}) - \theta_{-3\mathrm{dB_o}}|}{\theta_{-3\mathrm{dB_o}}}\right)k_1 \\ Z_2 = \begin{cases} 0, & \text{if } SLL_c(W_{m\times n}) > 13 \\ \frac{|SLL_c(W_{m\times n}) - SLL_0|}{SLL_0} & \text{if } SLL_c(W_{m\times n}) \le 13, \end{cases} \end{cases}$$

Algorithm 1: Beam Forming Algorithm in Single Beam Scenario

Input: (Λ, Φ), center of the beam in Latitude and longitude coordinates,
$\theta_{-3\text{dB}_\text{o}}$, desired beamwidth,
SLL_o, desired minimum SLL

Output: $W_{m\times n}$, Weight matrix based on previous inputs

Initiate: Population(W_o)
while Termination criteria not met **do**
  Calculate: Radiation Pattern $F(W_c)$
  Extract: $\theta^{\text{b}}_{-3\text{dB}_\text{c}}$, $\text{SLL}^{\text{b}}_{\text{c}}$
  Calculate: $\text{f}(Z_1(W_c) + Z_2(W_c))$
  if $f < f_{\text{min}}$ **then**
    Save: Optimal matrix $W = W_c$
    break
  else
    Select: Chromosomes based on fitnes
    Operations: CrossOver and Mutation
    Create: New Generation W_c
  end if
end while

and k_1 and k_2 are weights that determine the relative importance of achieving the desired beamwidth versus the side lobe level, and R is the number of cuts where the beamwidth will be assessed. The algorithm employed to compute the weight vector $W_{m\times n}$, crucial for achieving the desired beamwidth and SLL as defined in the cost function, is detailed in Algorithm 1.

To evaluate the performance of Algorithm 1, we established four scenarios, as detailed in Table 2. The primary objective in these scenarios was to achieve the specified beamwidth while maximizing the SLL. The results we obtained closely align with the desired outcomes, indicating a noticeable trend. We observed that increasing the beamwidth leads to a reduction in the total number of active antenna elements obtained by summing the ones inside W. Concurrently, the optimization process becomes more challenging in maintaining an optimal SLL. This phenomenon can be attributed to the inverse relationship between beamwidth and directivity: a wider beamwidth necessitates a less directive array. Consequently, this results in fewer active antenna elements, limiting the options available for effective antenna thinning. The results of the four scenarios are visually depicted in Figure 8. The results reveal several interesting and intuitive findings. Most notably, there is an inverse relationship between the number of elements and the beamwidth; as the beamwidth decreases, the number of elements correspondingly increases. Furthermore, the SLL approaches its limit when the number of active elements is reduced. Additionally, the algorithm faces increased challenges in meeting the requirements as the desired beamwidth is expanded. These findings will be discussed in more detail in the following subsection.

TABLE 2. Four beams scenario results in terms of θ_{-3dB}, SLL, and active elements.

Scenario.	θ_{-3dB_r} (°)	θ_{-3dB_o} (°)	SLL_c (dB)	SLL_o (dB)	Active Element
a)	9.13	9	16.84	>13	51
b)	12.975	13	15.78	>13	28
c)	16.081	16	13.97	>14	19
d)	16.7	18	13.67	>13	16

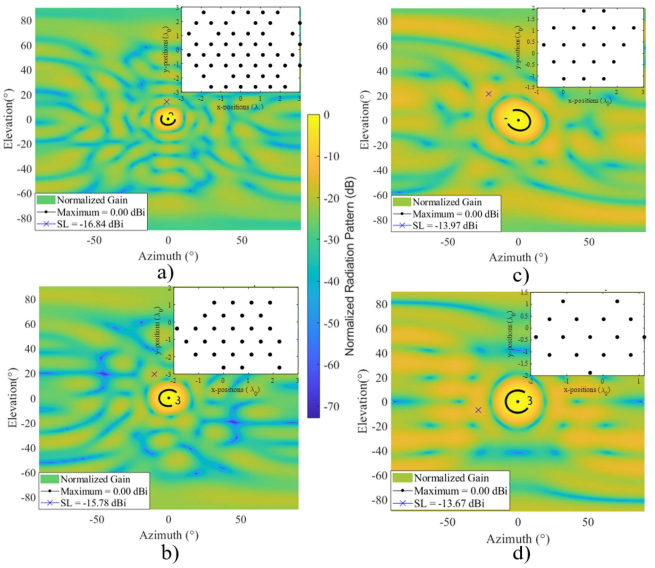

FIGURE 8. Radiation Patterns of the four scenarios presented in Table 2.

B. MULTIPLE BEAM SCENARIO

The concept of array thinning, which is typically applied to large arrays with over 200 elements, can be effectively utilized even in smaller arrays, as demonstrated in our scenario. However, the reduction in gain is more pronounced in smaller arrays as well as the degree of freedom in selecting the desired SLL. On the other hand, the key benefit of array thinning in a multi-beam regardless the total number of antenna elements lies in its contribution to the optimization process. It provides additional flexibility and degrees of freedom to achieve desired outcomes.

For instance, if we sum the weight matrices of the four described scenarios presented in the previous subsection and plot the results in the form of a colored dotted grid, as illustrated in Figure 9 we can reveal a discernible trend. In scenarios involving multiple beams, the array's central elements are predominantly active, diminishing progressively towards the edges. This pattern indicates a higher likelihood of central element activation when generating these beams. However, this leads to challenges such as uneven power distribution across the antenna elements, necessitating a complex heat dissipation strategy and managing the saturation levels of antenna power amplifiers.

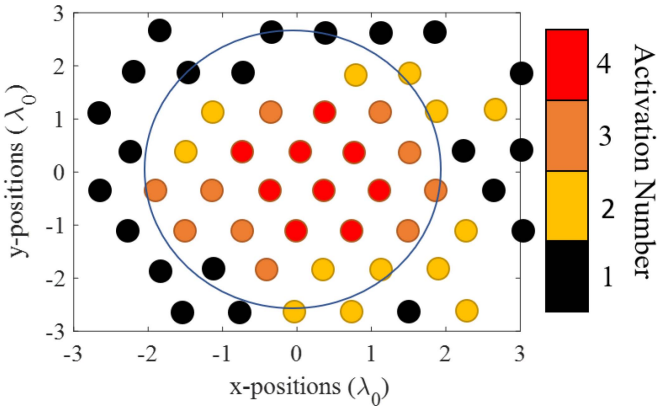

FIGURE 9. Activation times of the antenna elements presented in Figure 8.

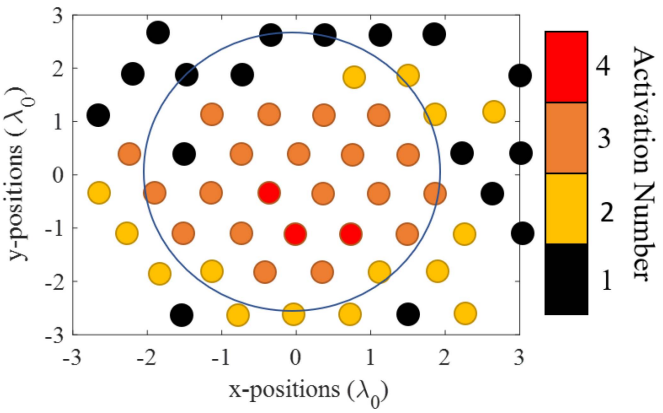

FIGURE 10. Activation times of the antenna elements presented in Figure 8 by shifting the positions of the antenna elements corresponding to the fourth beam.

To explore alternative strategies, as an example, we examined a deviation in the fourth beam scenario. Here, active elements were shifted two positions left and one position down, as shown in Figure 10. Remarkably, this adjustment maintained the integrity of the fourth radiation pattern while halving the activation frequency of the antenna elements. This result underscores the potential of an optimization process that finds suitable configurations to balance antenna element activation, especially when synthesizing beams with different constraints.

Consequently, in multi-beam configurations, it is advisable to integrate the instances of antenna element activation into the optimization parameters. This approach promotes a more balanced activation across the array, enhancing the system's overall performance and efficiency. Such optimization not only addresses the immediate concerns of power distribution and heat management but also contributes to the longevity and reliability of the antenna system.

Finally, as we can control the activation of the elements we can add another constraint based on the overall power consumption of the array to limit as much as possible the power consumption while maintaining a desired beamwidth.

The optimization problem for the multibeam scenario can be mathematically represented using Equation (16):

$$\begin{aligned} \min_{W^b} \; & f\left(\theta^b_{-3dB}(W^b), SLL^b(W^b)\right) \\ \text{subject to} \; & \sum_{b=1}^{B}\sum_{m=1}^{M}\sum_{n=1}^{N}|W^b_{m,n}|^2 \le p_{\max} \\ & \sum_{b=1}^{B}|W^b| \odot |W^b| \le P_{\max}, \end{aligned} \tag{16}$$

where f is the cost function and it is defined by Equation (17):

$$f\left(\theta^b_{-3dB}, SLL^b\right) = Z_1\left(W^b\right) + Z_2\left(W^b\right)$$

$$Z_1\left(W^b\right) = \frac{1}{B}\sum_{b=1}^{b}\frac{1}{R}\sum_{r=1}^{R}\frac{|\theta^b_{-3dB_r}(W^b) - \theta^b_{-3dB_0}(W^b)|}{\theta^b_{-3dB_0}(W^b)}$$

$$Z_2\left(W^b\right) = \begin{cases} 0, & \text{if } \mathrm{SLL}^b_c > 13 \\ \frac{1}{B}\sum_{b=1}^{B}\frac{|\mathrm{SLL}^b_c(W^b) - \mathrm{SLL}_0|}{\mathrm{SLL}_0}, & \text{if } \mathrm{SLL}^b_c \le 13 \end{cases} \tag{17}$$

where $\theta^b_{-3dB_0}$ is the desired -3 dB beamwidth per beam, $\theta^b_{-3dB_c}$ is the calculated -3 dB beamwidth per beam, SLL^b_0 is the overall desired SLL per beam, SLL^b_c is the calculated Side Lobe level per beam, W^b is the calculated weight matrix per beam, $p_{\max}$ is the maximum power of the array, and $P_{\max}$ is the maximum activation times per element matrix.

Following a genetic type of optimization, we derived Algorithm 2 to find the suitable weight matrices that satisfy the problem presented in Equation (16).

Essentially, the algorithm is an extension of the previous approach, now incorporating the activation instance for each element at $P_{\max}$ and the total power consumption of the DRA, denoted as $p_{\max}$, as constraints in the cost function calculation. This means that the algorithm aims to minimize the violation of these constraints as much as possible. Moreover, the gene calculation in each generation is treated holistically. This approach involves computing a variable that encapsulates all the genes of the weight vectors for each beam scenario, which are subsequently distributed to the corresponding beams. A more detailed process is depicted in Figure 11. It starts with the Genetic Algorithm (GA) generating a random initial solution. This solution is represented as a multidimensional matrix, consisting of dimensions (MxB), N, and C (Step a), where M is the number of rows, N the number of columns, B the number of beams, and C the total number of chromosomes. Each matrix is then subdivided into smaller matrices of dimensions Mxb, N, C, where 'b' represents the beam number. These smaller matrices are evaluated using a cost function, which calculates key metrics like beamwidth, SLL, activation instances, and overall power consumption. Next, the algorithm sorts these matrices based on the calculated cost values, arranging them from the lowest to the highest cost (Step b). The subsequent phase involves evolutionary optimization. The algorithm eliminates the less efficient half of the chromosomes and generates a new set. This new generation is created through

Algorithm 2: Beam Forming Algorithm in Multi Beam Scenario

Input: (Λ^b, Φ^b), center of the beam in Latitude and longitude coordinates per beam,
$\theta^{\mathrm{b}}_{-3\mathrm{dB_o}}$, required beamwidth per beam,
$p_{\max}$, maximum power consumption,
$P_{\max}$, Maximum activation times matrix,
$\mathrm{SLL}^{\mathrm{b}}_{\mathrm{o}}$, minimum SLL per beam,
Output: W^b, Weight matrix based on previous inputs
Data: Set of possible configurations on Satellite considering system constraints
Ensure: $\sum_{b=1}^{B} |W^b| \odot |W^b| \leq P_{\max}$
Ensure: $\sum_{b=1}^{B} \sum_{m=1}^{M} \sum_{n=1}^{N} |W^b_{m,n}|^2 \leq p_{\max}$

Initiate: Population(W^b_o)
while Termination criteria not met **do**
  Calculate: Antenna Pattern $F(W^b_c)$
  Extract: $\theta^{\mathrm{b}}_{-3\mathrm{dB_c}}$, $\mathrm{SLL}^{\mathrm{b}}_{\mathrm{c}}$, $p_{\max}$ and $P_{\max}$
  Calculate: $\mathrm{f}(Z_1(W^b_c) + Z_2(W^b_c))$
  if $f < f_{\min}$ **then**
    Save: Optimal matrix $W^b = W^b_c$
    break
  else
    Select: Chromosomes based on fitnes
    Operations: CrossOver and Mutation
    Create: New Generation W^b_c
  end if
end while

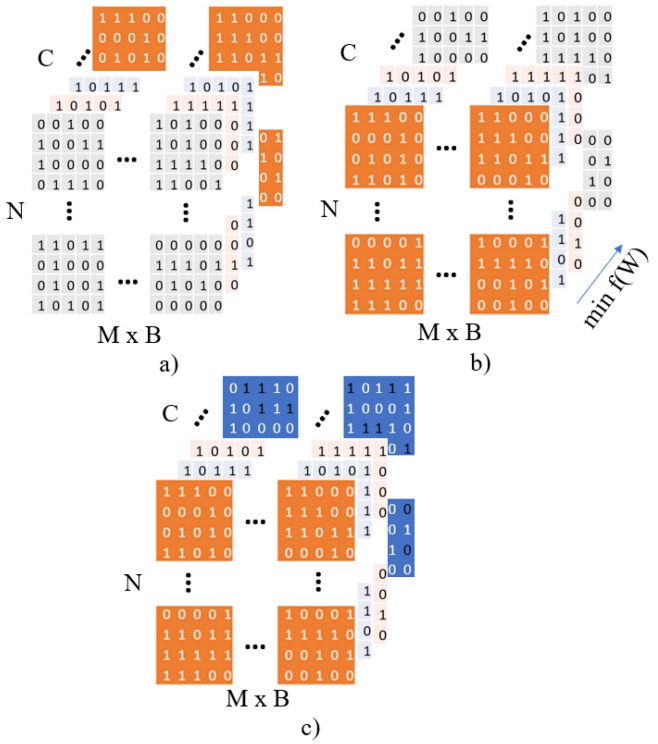

FIGURE 11. GA gene selection process. a) Original set of genes and chromosomes containing the value of *W* corresponding to each beam. b) Ordered Genes and Chromosomes based on the calculated cost function. c) Mutation of the best Chromosomes.

the crossover and mutation processes, applied to the more effective chromosomes (Step c). This iterative process continues until a chromosome is found whose cost function value falls below a predetermined threshold, in this case, 0.001. Alternatively, the process will conclude once a set number of iterations have been completed. This methodical approach ensures that the algorithm progressively evolves towards an optimal solution, balancing various parameters such as beamwidth, SLL, and power efficiency.

In the proposed multibeam scenario, the beams power layers are superimposed when generated concurrently. However, when phases are superimposed while operating on the same frequency, spatial separation of the beams becomes essential to avert beam deformation. To tackle this challenge, our strategy employs a multi-color approach, utilizing distinct frequency sub-bands and polarizations for generating each beam. This technique guarantees the preservation of each beam's integrity, effectively preventing interference and ensuring the maintenance of desired beam properties.

V. RESULTS

The proposed algorithm has undergone into an evaluation oriented to a CubeSat scenario, operating in a multi-beam environment within LEO. General characteristics of the evaluation setup include:

- *Geographical Positioning of the satellite:* The CubeSat is positioned at a latitude of 51° and a longitude of 7°.
- *Orbital Altitude of the satellite:* It orbits at an altitude of 500 km above the Earth's surface.
- *Available Power:* 10 W that will be distributed to the antenna power amplifier.
- *Power per element per beam:* $\frac{10}{7\times64}$ (Watts) that is calculated based on the available power divided by the number of beams and total elements.
- *SLL:* 13 (dB) is the $\mathrm{SLL_o}$ for any synthesized beam.
- *Geographical Positioning of the beam center:* latitude = [7°, 7.9676°, 6.0081°, 7.4354°, 6.5178°, 7.4354°, 6.5178°], longitude = [51° 51° 51° 51.733° 51.758° 50.267° 50.242°]
- *Required beamwidth* [10° 12.5° 12° 13° 11° 14.5° 9°]

Given the general characteristics of our evaluation setup, we conducted analyses across three distinct scenarios, each applying varying facets of the algorithm. These scenarios progressively increase in complexity, to demonstrate the efficacy of the algorithm, which starts with the most fundamental, termed the 'base scenario,' followed by the subsequent scenario, scenario #1, which introduces constraints in the computation. The final scenario, scenario #2, presents even more challenging constraints to address.

A. BASE SCENARIO

In the base scenario, the beam synthesis process is defined by general requirements. These requirements are outlined as follows:

TABLE 3. Characteristics of synthesized beams in the base scenario (no constraints).

Beam	θ_{-3dB_o} (°)	θ_{-3dB_c} (°)	error (%)	SLL (dB)	ActEle	Gain (dBi)	EIRP (dBm)
1	10	9.7797	2.2032	15.17	43	24.773	24.595
2	12.5	12.353	1.1795	15.49	28	22.887	20.846
3	12	11.693	2.5573	14.441	31	23.339	21.74
4	13	12.973	0.20661	13.785	26	22.569	20.206
5	11	11.155	1.4124	14.35	37	24.041	23.21
6	14.5	14.45	0.34371	13.034	20	21.474	17.971
7	9	9.1125	1.2503	14.283	51	25.46	26.023

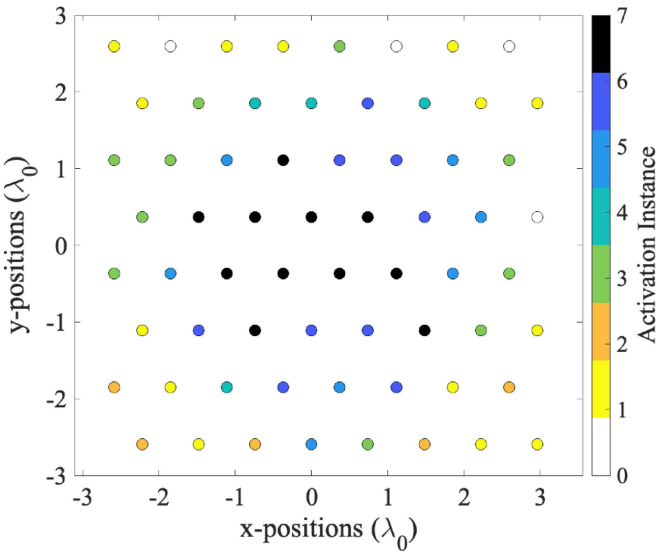

FIGURE 12. Activation instances in the DRA for the base scenario.

- *Activation instances:* This scenario does not impose any constraints on the number of activation instances.
- *Maximum power consumption:* There is no limitation or control over the maximum power consumption in this scenario.

Detailed results from the beam synthesis in this base scenario are presented in Table 3, which provides a comprehensive overview of the outcomes.

To visually understand the activation instances of each of the antenna elements in this scenario an illustration that overlaps the activation times of each element in the form of a different color is shown in Figure 12. Finally, The projection of the half-power beamwidths of the synthesized beams over the earth is depicted in Figure 13.

B. SCENARIO #1

In Scenario #1, the beam synthesis process is subject to specific requirements, as outlined below:

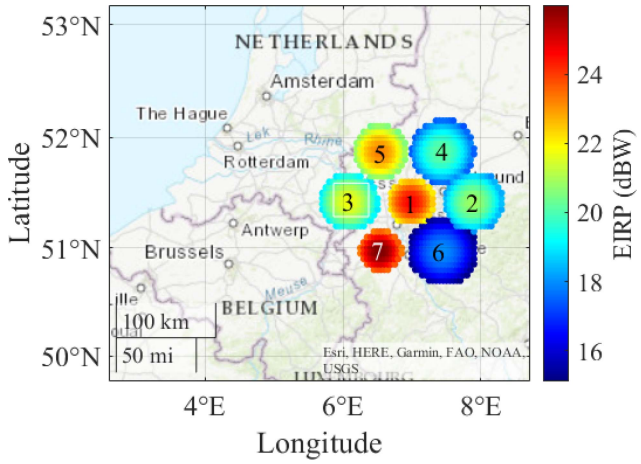

FIGURE 13. Half-power beamwidth projection over the earth of the synthesized beams corresponding to the base scenario.

TABLE 4. Characteristics of synthesized beams in the scenario #1.

Beam	θ_{-3dB_o} (°)	θ_{-3dB_c} (°)	error (%)	SLL (dB)	Act. Elem.	Gain (dBi)	EIRP (dBm)
1	10	9.8303	1.6971	13.597	26	22.742	20.379
2	12.5	12.416	0.67405	15.583	27	22.723	20.524
3	12	11.704	2.468	14.624	30	23.175	21.433
4	13	13.069	0.53397	13.749	23	22.075	19.18
5	11	11.162	1.4761	14.437	32	23.463	22.002
6	14.5	14.454	0.31574	14.596	21	21.665	18.375
7	9	9.0782	0.86852	14.545	44	24.858	24.78

- *Activation Instances:* A limit of a maximum of 6 activation instances out of 7 is imposed for any of the antenna elements.
- *Maximum Power Consumption:* This scenario does not implement control over the maximum power consumption, allowing for unrestricted power usage.

Detailed outcomes from the beam synthesis under these constraints are presented in Table 4.

The activation instances for each antenna element in Scenario #1 are depicted in Figure 14, and the corresponding projection over the earth of the half-power beamwidths for this scenario are shown in Figure 15.

C. SCENARIO #2: SPECIFIC CONSTRAINTS

Scenario #2 is characterized by distinct and more difficult to reach requirements for the beam synthesis process, which are as follows:

- *Activation Instances:* A constraint is placed on the activation instances, limiting them to a maximum of 5 out of 7 for any of the antenna elements.

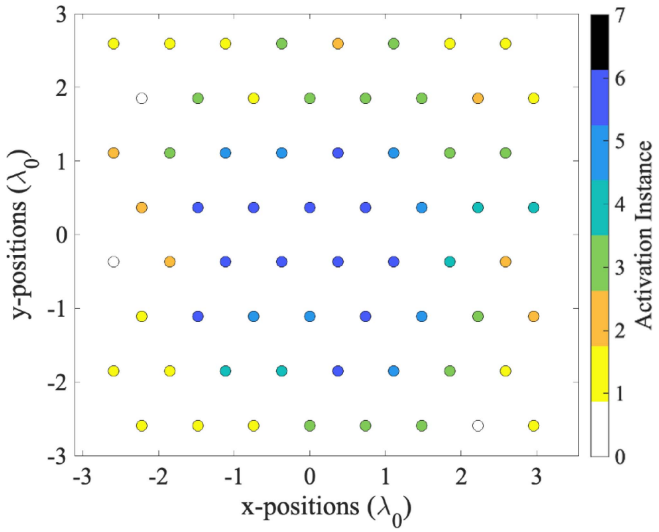

FIGURE 14. Activation Instances in Scenario #1.

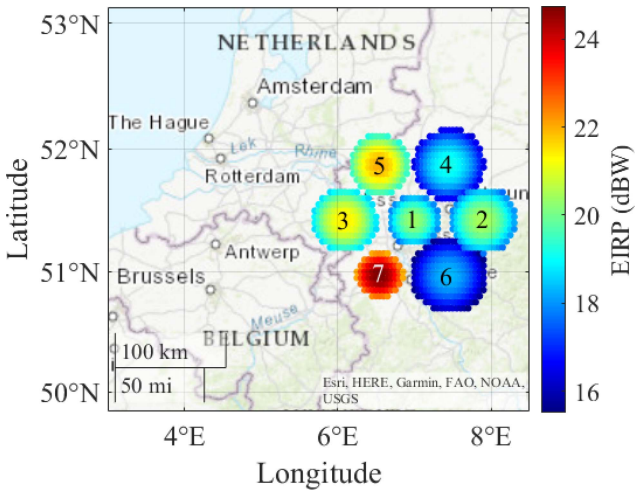

FIGURE 15. Half-power beamwidth projection of the synthesized Beam in Scenario #1.

- *Maximum Power Consumption:* There is stringent control over the overall power consumption, capped at a maximum of 1.2 W.

Detailed analyses and results from the beam synthesis under these specified conditions are comprehensively outlined in Table 5.

The activation instances of each of the antenna elements for the current scenario are illustrated in Figure 16 and the projection over the earth of the synthesized beams for this scenario in Figure 17.

D. RESULT ANALYSIS

1) GENERAL RESULT ANALYSIS

Upon analyzing the results from each scenario, we have discerned several trends and noteworthy outcomes. Examining the data in Tables 3, 4, and 5, it is noticeable that the beamwidth error exhibits minimal variation in the first two scenarios, while the third scenario shows a more pronounced,

TABLE 5. Characteristics of synthesized beams in scenario #2.

Beam	θ_{-3dB_o} (°)	θ_{-3dB_c} (°)	error (%)	SLL (dB)	ActEle	Gain (dBi)	EIRP (dBm)
1	10	9.722	2.7797	12.85	25	20.101	20.101
2	12.5	12.197	2.4219	13.982	24	19.564	19.564
3	12	11.756	2.0304	14.839	27	20.569	20.569
4	13	12.926	0.57073	13.066	20	17.948	17.948
5	11	11.092	0.83319	13.743	27	20.57	20.57
6	14.5	14.304	1.3516	13.109	19	17.549	17.549
7	9	9.1286	1.4291	14.452	35	22.849	22.849

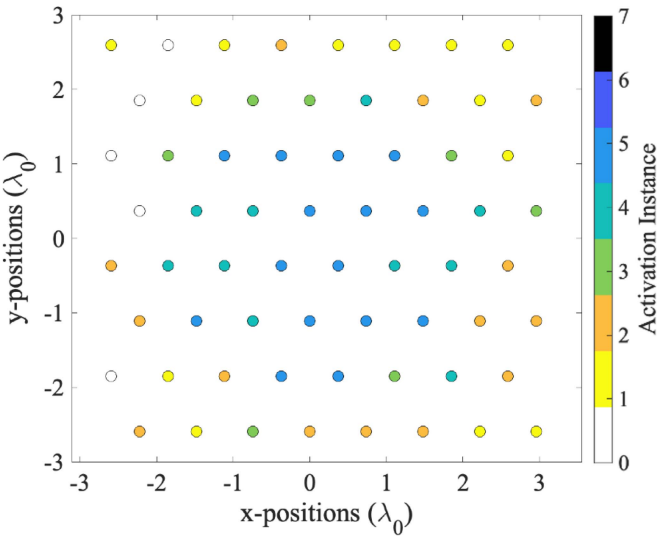

FIGURE 16. Activation instances for scenario #2.

yet still reasonable, fluctuation. This pattern can be attributed to the number of elements used for each beam, which limits the precision of beamwidth in all scenarios.

Additionally, the SLL values for each scenario tend to approach their limits as more activation instances are allowed for each antenna element reaching to not address the required value as is the case of Beam 1 in Scenario #2. This trend correlates with the number of elements needed to generate each beam and decreases as the beamwidth increases. This phenomenon is particularly noticeable in scenarios where the beamwidth is close to its lower limit. In such cases, to effectively address the requirements of SLL, the algorithm will require a greater number of elements, leading to the achievement of higher SLL values.

Another parameter that demonstrates a significant trend across the scenarios is the total gain and consequently, the EIRP. There is a noticeable downward trend in these values, likely due to array thinning. While the beamwidth may remain constant, directivity decreases due to the deactivation of elements. A more detailed analysis of the total elements

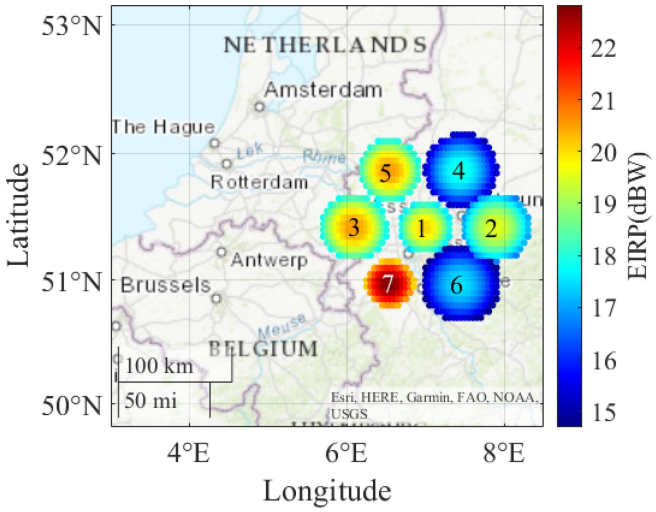

FIGURE 17. Half-power beamwidth projection of the synthesized beams for the scenario #2.

TABLE 6. Comparison between base scenario, scenario #1 and scenario #2.

Activation Instance	Base Scenario (# Antennas)	Scenario 1 (# Antennas)	Scenario 2 (# Antennas)
0	4	3	5
1	13	12	6
2	5	7	13
3	10	14	7
4	4	5	10
5	7	8	15
6	9	12	0
7	11	0	0
Power Consumption (dBm)	31.48	31.34	30.96

can be conducted by calculating the cumulative number of activation instances for each antenna element, as detailed in Table 6.

Upon closely analyzing the data presented in the table, it becomes apparent that the activation patterns of the antennas in the base scenario and Scenario #1 are remarkably similar, with 59 and 58 activations respectively. This similarity is primarily due to the lack of constraints on total power consumption in these scenarios, leading the algorithm to prioritize an equitable distribution of activation instances across the antenna array. Conversely, in Scenario #2, the number of active elements is noticeably reduced to 51. This decrease is a direct consequence of the unique constraint on maximum power consumption imposed in this scenario, which necessitates a more selective activation of elements to adhere to the power limitations.

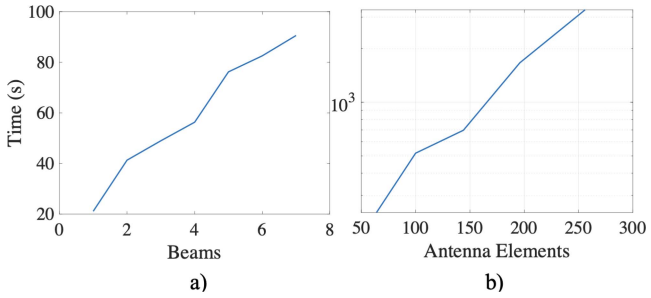

FIGURE 18. Time Analysis as the number of beams and antenna elements increases.

TABLE 7. Comparative table with related papers and the proposed approach in this work (TW).

Ref.	Beamwidth Control	SLL Control	Nulling Control	Power Control	Activation Control
[17]	Yes	Yes	No	Yes	No
[22]	Yes	Yes	Yes	Yes	No
[24]	Yes	Yes	No	No	No
[23]	Yes	Yes	Yes	No	No
[33]	Yes	Yes	No	No	No
TW	**Yes**	**Yes**	**No**	**Yes**	**Yes**

2) COMPLEXITY ANALYSIS

This work conducts a complexity analysis by utilizing the simulation time of the algorithm as a performance metric. We explore two distinct scenarios to illustrate the impact on computational complexity. In the first scenario, the focus is on the increase in the number of beams. Our results highlight a linear growth in simulation time corresponding to the increased number of beams, a relationship graphically represented in Figure 18a. Furthermore, to assess how the simulation time varies with a rising number of antenna elements, we establish a baseline with seven beams, and set the number of generations to 1600 and the chromosome count to 400, ensuring uniform computational parameters. The outcomes, depicted in Figure 18b, indicate that the computational time experiences an exponential increase as the number of antenna elements grows.

3) COMPARISON ANALYSIS

To conclude the analysis section, our approach is benchmarked against other similar studies in satellite communication systems that utilize array thinning techniques for designing specified beams, with constraints on required beamwidth, SLL, and power control. The comparative outcomes are detailed in Table 7.

4) RESULTS APPLICABILITY TO DIFFERENT BANDS AND PLATFORMS.

The applicability of this research work is valid across different frequency bands as long as it addresses some specific prerequisites. A fundamental prerequisite is the precise design of the unit cell to align with the operational frequency band. This is critical since we integrate the computed radiation pattern of the unit cell antenna into the

calculation process. Additionally, managing mutual coupling between unit cells is vital, with a target threshold of at least −20 dB. This particular requirement stems from the reliance on array factor calculations to deduce total antenna patterns, rather than employing full-wave simulations.

Moreover, this optimization strategy is versatile and can be adapted to different platforms without any inherent limitations, making it suitable for DRA operating in LEO, MEO, and GEO. The primary variable across these applications is the number of elements and the type of radiating element utilized, which will inevitably vary depending on the specific case. Furthermore, this approach is not just confined to space applications. It is equally applicable to terminals on the ground, supporting multi-beam functionalities for diverse applications such as terrestrial base stations, automotive radar systems, and space debris identification.

VI. CONCLUSION

This paper introduced an algorithm designed for synthesizing beam patterns in single and multi-beam scenarios using GA, taking into account parameters such as beamwidth, SLL, element activation instances, and available power. Through comprehensive analysis and simulations, we have shown the algorithm's capability to evenly distribute activation instances in a multi-beam scenario and to effectively perform beamforming. A key finding of our study is the algorithm's ability to prevent saturation in the central antenna elements, which are more prone to activation in multi-beam configurations.

A notable aspect of our research is the ground-up design of the proposed DRA, starting from dimensioning for a LEO environment to ensure minimum coverage area, and culminating in the development of an algorithm for generating desired beam patterns with even activation of antenna elements. This comprehensive approach provides a potential framework for the dimensioning, design, and beamforming of DRAs, applicable not only in LEO but also in GEO and other NGSO scenarios. Moreover, our methodology is scalable to scenarios with an unlimited number of beams and antenna elements, which could significantly reduce costs associated with power amplifiers and heat dissipation mechanisms.

While our results are promising, they also pave the way for future research. Potential avenues include exploring sector activation antenna instances, EIRP control, null steering, and application to regular arrays. Such future work could further enhance the versatility and efficiency of beamforming technologies in various communication scenarios.

ACKNOWLEDGMENT

Please note that the views of the authors of this paper do not necessarily reflect the views of ESA.

REFERENCES

[1] N. Chahat, *CubeSat Antenna Design*. Hoboken, NJ, USA: Wiley, 2021.
[2] A. Nascetti, E. Pittella, P. Teofilatto, and S. Pisa, "High-gain S-band patch antenna system for earth-observation cubesat satellites," *IEEE Antennas Wireless Propag. Lett.*, vol. 14, pp. 434–437, 2014.
[3] S. K. Podilchak, D. Comite, B. K. Montgomery, Y. Li, V. G.-G. Buendia, and Y. M. Antar, "Solar-panel integrated circularly polarized meshed patch for cubesats and other small satellites," *IEEE Access*, vol. 7, pp. 96560–96566, 2019.
[4] O. F. G. Palacios, R. E. D. Vargas, J. A. H. Perez, and S. B. C. Erazo, "S-band koch snowflake fractal antenna for cubesats," in *Proc. IEEE ANDESCON*, 2016, pp. 1–4.
[5] S. Zarbakhsh, M. Akbari, M. Farahani, A. Ghayekhloo, T. A. Denidni, and A.-R. Sebak, "Optically transparent subarray antenna based on solar panel for cubesat application," *IEEE Trans. Antennas Propag.*, vol. 68, no. 1, pp. 319–328, Jan. 2020.
[6] R. M. Rodríguez-Osorio, and E. F. Ramírez, "A hands-on education project: Antenna design for inter-cubesat communications [education column]," *IEEE Antennas Propag. Mag.*, vol. 54, no. 5, pp. 211–224, Oct. 2012.
[7] S. X. Ta, V. D. Le, K. K. Nguyen, and C. Dao-Ngoc, "Planar circularly polarized X-band array antenna with low sidelobe and high aperture efficiency for small satellites," *Int. J. RF Microw. Comput.-Aided Eng.*, vol. 29, no. 11, 2019, Art. no. e21914.
[8] P. A. Warren, J. W. Steinbeck, R. J. Minelli, and C. Mueller, *Large, Deployable S-Band Antenna for a 6U Cubesat*, Phys. Sci. Inc., Andover, MA, USA, 2015.
[9] N. Chahat, R. E. Hodges, J. Sauder, M. Thomson, E. Peral, and Y. Rahmat-Samii, "Cubesat deployable Ka-band mesh reflector antenna development for earth science missions," *IEEE Trans. Antennas Propag.*, vol. 64, no. 6, pp. 2083–2093, Jun. 2016.
[10] G. Buttazzoni, M. Comisso, A. Cuttin, M. Fragiacomo, R. Vescovo, and R. V. Gatti, "Reconfigurable phased antenna array for extending cubesat operations to Ka-band: Design and feasibility," *Acta Astronautica*, vol. 137, pp. 114–121, Aug. 2017.
[11] J. Klein, J. Hawkins, and D. Thorsen, "Improving cubesat downlink capacity with active phased array antennas," in *Proc. IEEE Aerosp. Conf.*, 2014, pp. 1–8.
[12] R. E. Hodges, N. Chahat, D. J. Hoppe, and J. D. Vacchione, "A deployable high-gain antenna bound for mars: Developing a new folded-panel reflectarray for the first cubesat mission to mars," *IEEE Antennas Propag. Mag.*, vol. 59, no. 2, pp. 39–49, Apr. 2017.
[13] Y.-S. Chen, Y.-H. Wu, and C.-C. Chung, "Solar-powered active integrated antennas backed by a transparent reflectarray for cubesat applications," *IEEE Access*, vol. 8, pp. 137934–137946, 2020.
[14] M. J. Veljovic and A. K. Skrivervik, "Circularly polarized transmitarray antenna for cubesat intersatellite links in K-band," *IEEE Antennas Wireless Propag. Lett.*, vol. 19, pp. 1749–1753, 2020.
[15] R. J. Mailloux, *Phased Array Antenna Handbook*, 3rd ed. Norwood, MA, USA: Artech House, 2018.
[16] Y. Lo, "A mathematical theory of antenna arrays with randomly spaced elements," *IEEE Trans. Antennas Propag.*, vol. 12, no. 3, pp. 257–268, May 1964.
[17] J. A. Vásquez-Peralvo et al., "Genetic algorithm-based beamforming in subarray architectures for geo satellites," 2023, *arXiv:2311.01366*.
[18] W.-T. Li, X.-W. Shi, and Y.-Q. Hei, "An improved particle swarm optimization algorithm for pattern synthesis of phased arrays," *Progr. Electromagn. Res.*, vol. 82, pp. 319–332, Jan. 2008.
[19] A. Khzmalyan and A. Kondratiev, "The phase-only shaping and adaptive nulling of an amplitude pattern," *IEEE Trans. Antennas Propag.*, vol. 51, no. 2, pp. 264–272, Feb. 2003.
[20] C.-J. Lu, W.-X. Sheng, Y.-B. Han, and X.-F. Ma, "A novel adaptive phase-only beamforming algorithm based on semidefinite relaxation," in *Proc. IEEE Int. Symp. Phased Array Syst. Technol.*, 2013, pp. 617–621.
[21] B. Boustani, A. Baghdad, A. Sahel, A. Badri, and A. Ballouk, "Adaptive algorithm for smart antenna system," in *Proc. 6th Int. Conf. Multimedia Comput. Syst. (ICMCS)*, 2018, pp. 1–5.
[22] J. A. Vásquez-Peralvo et al., "Flexible beamforming for direct radiating arrays in satellite communications," *IEEE Access*, vol. 11, pp. 79684–79696, 2023.
[23] J. Mayhan, "Thinned array configurations for use with satellite-based adaptive antennas," *IEEE Trans. Antennas Propag.*, vol. 28, no. 6, pp. 846–856, Nov. 1980.
[24] R. Gal and R. Shavit, "Thinning satellite communication antenna arrays for dual band operation," in *Proc. IEEE Int. Conf. Sci. Electr. Eng. Israel (ICSEE)*, 2018, pp. 1–5.

[25] K. Chen, X. Yun, Z. He, and C. Han, "Synthesis of sparse planar arrays using modified real genetic algorithm," *IEEE Trans. Antennas Propag.*, vol. 55, no. 4, pp. 1067–1073, Apr. 2007.
[26] K. Chen, H. Chen, L. Wang, and H. Wu, "Modified real GA for the synthesis of sparse planar circular arrays," *IEEE Antennas Wireless Propag. Lett.*, vol. 15, pp. 274–277, 2016.
[27] J. S. Petko and D. H. Werner, "Pareto optimization of thinned planar arrays with elliptical mainbeams and low sidelobe levels," *IEEE Trans. Antennas Propag.*, vol. 59, no. 5, pp. 1748–1751, May 2011.
[28] G. Caille, Y. Cailloce, C. Guiraud, D. Auroux, T. Touya, and M. Masmousdi, "Large multibeam array antennas with reduced number of active chains," in *Proc. Eur. Conf. Antennas Propag.*, 2007, pp. 1–9.
[29] R. L. Haupt, "Interleaved thinned linear arrays," *IEEE Trans. Antennas Propag.*, vol. 53, no. 9, pp. 2858–2864, Sep. 2005.
[30] L. Poli, P. Rocca, M. Salucci, and A. Massa, "Reconfigurable thinning for the adaptive control of linear arrays," *IEEE Trans. Antennas Propag.*, vol. 61, no. 10, pp. 5068–5077, Oct. 2013.
[31] R. L. Haupt, "Adaptively thinned arrays," *IEEE Trans.Antennas Propag.*, vol. 63, no. 4, pp. 1626–1632, Apr. 2015.
[32] J. A. Vásquez-Peralvo, J. M. Fernández-González, J. M. Rigelsford, and P. Valtr, "Interwoven hexagonal frequency selective surface: An application for WiFi propagation control," *IEEE Access*, vol. 9, pp. 111552–111566, 2021.
[33] Y. Cailloce, G. Caille, I. Albert, and J. M. Lopez, "A Ka-band direct radiating array providing multiple beams for a satellite multimedia mission," in *Proc. IEEE Int. Conf. Phased Array Syst. Technol.*, 2000, pp. 403–406.

JUAN ANDRÉS VÁSQUEZ-PERALVO (Member, IEEE) was born in Quito, Ecuador. He received the B.Eng. degree in electronics and telecommunications from the Escuela Politécnica Nacional, Quito, the M.Sc. degree in wireless communication systems from The University of Sheffield, Sheffield, U.K., and the Ph.D. degree in communication systems from the Universidad Politécnica de Madrid, Madrid, Spain. He is currently a Postdoctoral Fellow with the Université du Luxembourg in antenna design for satellite communications. His current research interests are phase array design for satellite communications, metasurfaces, additive manufacturing, and lens antenna design.

JORGE QUEROL (Member, IEEE) was born in Forcall, Castelló, Spain, in 1987. He received the B.Sc. (+5) degree in telecommunication engineering, the first M.Sc. degree in electronics engineering, the second M.Sc. degree in photonics, and the Ph.D. degree (cum laude) in signal processing and communications from the Universitat Politecnica de Catalunya—BarcelonaTech (UPC), Barcelona, Spain, in 2011, 2012, 2013, and 2018, respectively. His Ph.D. thesis was devoted to the development of novel anti-jamming and counter-interference systems for global navigation satellite systems (GNSS), GNSS-Reflectometry, and microwave radiometry. One of his outstanding achievements was the development of a real-time standalone precorrelation mitigation system for GNSS, named FENIX, in a customized software-defined radio (SDR) platform. FENIX was patented, licensed, and commercialized by MITIC Solutions, a UPC spin-off company. Since 2018, he has been with the SIGCOM Research Group, Interdisciplinary Centre for Security, Reliability, and Trust (SnT), University of Luxembourg, Luxembourg, and the Head of the Satellite Communications Laboratory. He is involved in several ESA and Luxembourgish national research projects dealing with signal processing and satellite communications. His research interests include SDR, real-time signal processing, satellite communications, 5G nonterrestrial networks, satellite navigation, and remote sensing. He received the Best Academic Record Award of the year in Electronics Engineering at UPC in 2012, the First Prize of the European Satellite Navigation Competition Barcelona Challenge from the European GNSS Agency in 2015, the Best Innovative Project of the Market Assessment Program of EADA Business School in 2016, the Award Isabel P. Trabal from Fundacióó Caixa d'Enginyers for its quality research during his Ph.D. in 2017, and the Best Ph.D. Thesis Award in remote sensing in Spain from the IEEE Geoscience and Remote Sensing Spanish Chapter in 2019.

FLOR ORTÍZ (Member, IEEE) received the B.S. degree in telecommunications engineering and the M.S. degree in electrical engineering-telecommunications from the Universidad Nacional Autónoma de México, Mexico City, Mexico, in 2015 and 2016, respectively, and the Ph.D. degree in telecommunications engineering from the Universidad Politécnica de Madrid, Madrid, Spain, in 2021. Her Ph.D. thesis focused on optimizing the design of very high-throughput satellite systems, especially optimizing the cost per Gb/s in orbit and managing radio resources for flexible payloads using different machine learning techniques, especially those based on reinforcement learning and supervised learning. During her Ph.D. (in 2019), she performed a research period with the University of Bologna, Italy. She is a Research Associate with the Interdisciplinary Center for Security, Reliability, and Trust (SnT), University of Luxembourg. Her research interests focus on implementing innovative machine learning techniques for operations in satellite communication systems.

JORGE LUIS GONZÁLEZ RIOS (Member, IEEE) received the B.S. (with Hons.), M.S., and Ph.D. degrees in telecommunications and electronics from the Technological University of Havana (CUJAE), Cuba, in 2006, 2009, and 2018, respectively. He is with the Interdisciplinary Centre for Security, Reliability and Trust (SnT), University of Luxembourg. From September 2006 to July 2019, he was a Lecturer and a Researcher with the Research Center on Microelectronics (CIME), CUJAE. He visited the Seville Institute of Microelectronics (IMSE-CNM), Spain, from 2010 to 2012, and the Group of Microelectronics, Federal University of Itajuba (UNIFEI), Brazil, in 2013. His research interests include RF/analog circuits, embedded systems, and wireless and satellite communications.

EVA LAGUNAS (Senior Member, IEEE) received the M.Sc. and Ph.D. degrees in telecommunications engineering from the Polytechnic University of Catalonia (UPC), Barcelona, Spain, in 2010 and 2014, respectively. She was a Research Assistant with the Department of Signal Theory and Communications, UPC from 2009 to 2013. In 2009, she was a Guest Research Assistant with the Department of Information Engineering, University of Pisa, Italy. From November 2011 to May 2012, she was a Visiting Researcher with the Center for Advanced Communications, Villanova University, Villanova, PA, USA. In 2014, she joined the Interdisciplinary Centre for Security, Reliability and Trust (SnT), University of Luxembourg, where she is currently a Research Scientist. Her research interests include radio resource management and general wireless networks optimization.

LUIS MANUEL GARCÉS-SOCORRÁS (Member, IEEE) received the B.S. degree in automation control engineering, the M.S. degree in digital systems, and the Ph.D. degree in electronics from the Technological University of Havana, Cuba, in 2006, 2011, and 2017, respectively. From September 2008 to March 2022, he was a Lecturer and a Researcher with the Automation and Computing Department, Technological University of Havana. In 2010, 2011, and 2013, he was a Visiting Researcher with the Seville Institute of Microelectronics (IMSE-CNM), Spain, and from September 2014 to March 2015, he was a Visiting Researcher with the Group of Microelectronics, Federal University of Itajuba (INIFEI), Brazil, as well as from September to December 2017, as a Postdoctoral Researcher. Since April 2022, he has been a Research and Development Specialist with the Interdisciplinary Centre for Security, Reliability and Trust, University of Luxembourg. His research activity includes digital signal processing, FPGAs, and embedded systems implementations of satellite communication applications.

JUAN CARLOS MERLANO DUNCAN (Senior Member, IEEE) received the Diploma degree in electrical engineering from the Universidad del Norte, Barranquilla, Colombia, in 2004, and the M.Sc. and Ph.D. Diploma (cum laude) degrees from the Universitat Politècnica de Catalunya (UPC), Barcelona, Spain, in 2009 and 2012, respectively. His research interests are wireless communications, remote sensing, distributed systems, frequency distribution and carrier synchronization systems, software-defined radios, and embedded systems. At UPC, he was responsible for the design and implementation of a radar system known as SABRINA, which was the first ground-based bistatic radar receiver using space-borne platforms, such as ERS-2, ENVISAT, and TerraSAR-X as opportunity transmitters (C and X bands). He was also in charge of the implementation of a ground-based array of transmitters, which was able to monitor land subsidence with subwavelength precision. These two implementations involved FPGA design, embedded programming, and analog RF/Microwave design. In 2013, he joined the Institute National de la Recherche Scientifique, Montreal, Canada, as a Research Assistant in the design and implementation of cognitive radio networks employing software development and FPGA programming. He has been with the University of Luxembourg since 2016, where he currently works as a Research Scientist leading the COMMLAB Laboratory, SIGCOM Group working on the SDR implementation of satellite and terrestrial communication systems.

MARCELE O. K. MENDONÇA (Member, IEEE) was born in Mesquita, Brazil. She received the Telecommunications Engineering degree from the Fluminense Federal University (UFF) in 2016, and the M.Sc. and Ph.D. degrees from the Signal Multimedia and Telecommunications Laboratory, Federal University of Rio de Janeiro in 2018 and 2022, respectively. She was a Ph.D. Visiting Scholar by the Swiss Government Excellence Scholarships Program with LTS4 Research Group, Ecole Polytechnique Fédérale de Lausanne, Switzerland, from 2021 to 2022 supervised by Prof. Pascal Frossard. She joined the Interdisciplinary Centre for Security, Reliability, and Trust, University of Luxembourg as a Research Associate in 2022. Her research interests are mainly signal processing, OFDM systems with reduced redundancy, massive MIMO systems with low complexity antenna selection to reduce transmission power, and machine learning for wireless communications, including robust systems based on adversarial learning. She was the 2nd place in the UFF Vasconcellos Torres Award of Scientific Initiation with the Project OFDM Systems in Software Gnuradio using USRP in 2014. Moreover, she received the Best Demo Award at the Brazilian Telecom Symposium with the Project FM Transmission and Reception Using Software-Defined Radios in 2019.

SYMEON CHATZINOTAS (Fellow, IEEE) received the M.Eng. degree in telecommunications from the Aristotle University of Thessaloniki, Thessaloniki, Greece, in 2003, and the M.Sc. and Ph.D. degrees in electronic engineering from the University of Surrey, Guildford, U.K., in 2006 and 2009, respectively. He is currently a Full Professor, and the Deputy Head of the SIGCOM Research Group, Interdisciplinary Centre for Security, Reliability, and Trust, University of Luxembourg, Esch-sur-Alzette, Luxembourg, and a Visiting Professor with the University of Parma, Parma, Italy. His research interests include multiuser information theory, cooperative/cognitive communications, and wireless network optimization. He has been involved in numerous research and development projects with the Institute of Informatics Telecommunications, National Center for Scientific Research Demokritos, Institute of Telematics and Informatics, Center of Research and Technology Hellas, and Mobile Communications Research Group, Center of Communication Systems Research, University of Surrey. He has coauthored more than 400 technical papers in refereed international journals, conferences, and scientific books. He was the co-recipient of the 2014 IEEE Distinguished Contributions to Satellite Communications Award, the CROWNCOM 2015 Best Paper Award, and the 2018 *EURASIP Journal on Wireless Communications and Networking* Best Paper Award. He is currently on the editorial board of the IEEE OPEN JOURNAL OF VEHICULAR TECHNOLOGY and the *International Journal of Satellite Communications and Networking*.